Measuring the temperature and profiles of Lyman-α absorbers

Garzilli, A.; Theuns, T.; Schaye, J.

MNRAS **000**, 000–000 (0000) Preprint 22 August 2018 Compiled using MNRAS LATEX style file v3.0

Measuring the temperature and profiles of Lyman-α absorbers

Antonella Garzilli[1⋆], Tom Theuns[2] and Joop Schaye[3]
[1] *Discovery Center, Niels Bohr Institute, Copenhagen University, Blegdamsvej 17, DK-2100 Copenhagen, Denmark*
[2] *Institute for Computational Cosmology, Department of Physics, Durham University, DH1 3LE Durham, UK*
[3] *Leiden Observatory, Leiden University, PO Box 9513, 2300 RA Leiden, The Netherlands*

Accepted –. Received –; in original form –

ABSTRACT
The distribution of the absorption line broadening observed in the Lyα forest carries information about the temperature and widths of the filaments in the intergalactic medium (IGM). In this work, we present and test a new method for inferring the temperature of the IGM, the size of the absorbing filaments and the photo-ionization rate of hydrogen from the properties of absorption line broadening in the Lyα forest. We apply our method to mock spectra from the reference model of the EAGLE cosmological simulation, and we demonstrate that we are able to reconstruct the IGM properties. Our method explicitly takes into account the degeneracy between IGM temperature, the photo-ionization rate of hydrogen and the widths of the intergalactic filaments.

Key words: intergalactic medium – quasars: absorption lines – large scale structure of Universe – methods: data analysis

1 INTRODUCTION

In the ΛCDM model of cosmology the Universe emerges from inflation in a quasi-homogeneous state, with small fluctuations in the density field of matter. From these initial conditions, the Universe evolves to its current state and becomes populated with structures such as galaxies and galaxy clusters. Most of the baryons do not reside in these dense structures, but in a diffuse medium that fills intergalactic space, called the intergalactic medium (IGM), that is organized in a network of sheets and filaments. The chemical composition of the IGM is mostly primordial, with a minor component of metals, produced by stars and likely injected in the IGM by galactic winds and outflows. Although Cantalupo et al. (2014) have reported that the IGM can be observed in emission, it has mainly been observed in absorption, in the spectra from distant and bright sources, such as quasars. The lack of the Gunn-Perterson trough (Gunn & Peterson 1965) since $z \sim 5$ implies that the IGM is in a highly ionized state. According to the current understanding of structures formation, the IGM is photo-ionized and photo-heated by an hydrogen-ionizing radiation background (UVB) originating from galaxies and quasars (e.g. Haardt & Madau 1996).

Hence, the IGM is observable through the absorption of light emitted by distant bright objects, through the Lyα forest, which is the collection of Lyα absorption lines. The Lyα forest is also fluctuating Gunn-Petersen absorption, because the absorption traces the fluctuations in the underlining neutral hydrogen density field. The widths of the lines in the Lyα forest are determined by the clustering of the absorbers and their temperature. For a review we refer the interested reader to Meiksin (2009). To gain information on the timing of reionization and the nature of the responsible sources, it is important to determine the IGM temperature. Moreover, the IGM temperature is an astrophysical bias in the study of the nature of dark matter at the smallest scales (Seljak et al. 2006; Garzilli et al. 2017).

Many groups have tried to measure the IGM temperature with different methods, using Voigt-profile fitting (Schaye et al. 1999; Schaye et al. 2000; Ricotti et al. 2000; McDonald et al. 2001; Bolton et al. 2012; Rudie et al. 2012; Hiss et al. 2017), studying the flux PDF (Theuns et al. 2000; Bolton et al. 2008; Viel et al. 2009; Calura et al. 2012; Garzilli et al. 2012), the flux power spectrum, wavelet analysis and curvature method (Theuns et al. 2000; Theuns & Zaroubi 2000; Zaldarriaga et al. 2001; Viel & Haehnelt 2006; Lidz et al. 2010; Becker et al. 2011; Garzilli et al. 2012). The details of the results from the different methods vary, but there is a general consensus that in the redshift interval between 2 and 4, $5000\,\mathrm{K} < T_0 < 30000\,\mathrm{K}$, where $\Delta = \rho/\langle\rho\rangle$ is the overdensity and $T_0 = T(\Delta = 1)$ is the temperature of the IGM at the cosmic mean density.

The width of the structures causing the absorption has been measured for the first time from pairs of quasars by Rorai et al. (2017). The intensity of the photo-ionizing background, $\Gamma_{\rm HI}$, has been measured by previous authors (Rauch et al. 1997; McDonald & Miralda-Escudé 2001; Meiksin & White 2004; Bolton et al. 2005; Kirkman et al. 2005; Faucher-Giguère et al. 2008), but always assuming a specific thermal history for the IGM, (see Fumagalli et al. (2017) for a measurement of the ultraviolet background at low redshift that is independent of the IGM). Over the redshift interval between 2 and 4, the measurements agree in finding $2 \times 10^{-13}\,\mathrm{s}^{-1} \leqslant \Gamma_{\rm HI} \leqslant 2 \times 10^{-12}\,\mathrm{s}^{-1}$.

As already pointed out by Hui et al. (1997), there are at least

⋆ E-mail: garzilli@nbi.ku.dk

two distinct physical effects that contribute to the minimum line broadening in the Lyα forest[1]: the first is the thermal Doppler effect, that is set by the temperature of the IGM, the second is the extent of the filaments in the IGM – the filaments are not virialized structures and there is a contribution of the differential Hubble flow across the absorbers (Gnedin & Hui 1998; Theuns et al. 2000; Schaye 2001; Desjacques & Nusser 2005; Peeples et al. 2010; Rorai et al. 2013; Garzilli et al. 2015b; Kulkarni et al. 2015). The simulations of Schaye et al. (1999) and Ricotti et al. (2000) showed that the minimum line broadening as a function of overdensity can be approximated by a power-law. In Garzilli et al. (2015b), we demonstrated that, under the hypothesis of a photo-ionized IGM, the lower envelope of the line broadening distribution is a convex function of the baryon density, and hence of the neutral hydrogen column density. We introduced an analytical description for the minimum amount of line broadening present in the Lyα forest. In this same work, we introduced the 'peak decomposition' of the neutral hydrogen optical depth, which differs from the standard Voigt profile fitting of the spectra described by eg. Carswell et al. (1987).

In this work, we present a new method for measuring the properties of the IGM from quasar absorption spectra, considering only the Lyα forest for each quasar spectrum. We develop the method using mock sightlines extracted from hydrodynamical simulations.

This paper is organized as follows. In Section 2, we describe the reference EAGLE simulation, from which we have extracted the mock spectra. In Section 3, we discuss the analytical description of the line broadening we use in this method, and the modifications with respect to the equations presented in Garzilli et al. (2015b). In Section 4, we discuss the reconstruction of the line broadening in the case of spectra with noise. In Section 4.2 we discuss the ability of our method to correctly constrain the IGM parameters from quasar spectra with noise. In Section 5, we present our conclusions. In Appendix A, we compare with Voigt profile fitting, which has been used widely in previous works. In Appendix B, we will show that our conclusions do not change in the case of lower signal to noise spectra: in this case we merely obtain larger error bars on the estimated parameters.

2 SIMULATIONS

2.1 The EAGLE simulations and the T/Δ relation

In this paper, we use the 25 cMpc (co-moving Mpc) high-resolution reference simulation of the EAGLE suite (Schaye et al. 2015; Crain et al. 2015; McAlpine et al. 2016), labelled 'L0025N0752' in table 2 of Schaye et al. (2015). The simulation is based on the Planck Collaboration et al. (2014) values of the cosmological parameters, and the initial baryonic particle mass is 1.81×10^6 M$_\odot$. This cosmological smoothed particle hydrodynamics (SPH) simulation is performed using the GADGET-3 incarnation of the code described by Springel (2005), with modifications to the hydrodynamics algorithm referred to as ANARCHY (described in the Appendix A of Schaye et al. (2015), see also Schaller et al. 2015). The reference model incorporates a set of sub-grid models to account for unresolved physics, which include star formation, energy feedback and mass loss feedback from stars, black halo formation, accretion and merging, and thermal feedback from accreting black holes. The parameters that encode these sub-grid models are calibrated to observations of $z \sim 0$ galaxies, namely the galaxy stellar mass function, galaxy sizes, and the stellar mass - black holes mass relation, as described in detail by Crain et al. (2015).

The simulation also accounts for photo-heating and radiative cooling in the presence of the imposed background of UV, X-ray and CMB radiation described by Haardt & Madau (2001), using the interpolation tables computed by Wiersma et al. (2009a). The optically-thin limit is assumed in these simulations.

Photo-heating and radiative cooling, adiabatic cooling due to the expansion of the Universe, and shocks from structure formation and feedback, result in a range of temperatures, T, for cosmic gas at any given density. However, there is a well defined minimum value of T at a given over-density $\Delta \equiv \rho/\bar{\rho}$. In the following, we will refer to this minimum value as the temperature-density relation (TDR for short). At $\Delta \leqslant 3$, the TDR is set by the interplay between photo-heating and adiabatic cooling, resulting in an approximately power law relation $T = T_0\,\Delta^{\gamma-1}$ (Hui & Gnedin 1997; Theuns et al. 1998; Sanderbeck et al. 2016). When the temperature of the cosmic gas is increased rapidly by photo-heating, as happens during reionisation, the slope is $\gamma \approx 1$, whereas asymptotically long after reionisation, it becomes $\gamma \approx 1 + 1/1.7 \approx 1.6$, as discussed by Hui & Gnedin (1997) and Theuns et al. (1998). The fact that γ in this limiting case is close to that of the adiabatic index of a mono-atomic gas, $\gamma = 5/3$, is a coincidence.

At higher overdensity, T is set by the balance between photo-heating and radiative cooling. This causes a gentle turn-over in the $T - \Delta$ relation around $\Delta = 3$ at redshift $z > 1$ (above $\Delta \approx 30$ at $z = 0.5$). In this work we will consider the simple case that the $T - \Delta$ relation is a power-law, and we leave the investigation of more physically motivated $T - \Delta$ relations for future work.

2.2 Mock sightlines

We compute mock sightlines from the EAGLE simulation. We begin by sampling the simulation volume with sightlines parallel to its z-axis, using pixels of velocity width $W_v = 1.4$ km s^{-1}, which is small enough to resolve any absorption features. We next use the interpolation tables from Wiersma et al. (2009b) to compute the neutral hydrogen fraction for each SPH particle in the optically-thin limit, taking the cosmic gas to be photo-ionised at the rate calculated by Haardt & Madau (2001). We then compute the contribution of each gas particle by integrating a kernel over each pixel, calculating the H I density, and the H I-weighted temperature and peculiar velocity. This is similar to the algorithm described in the Appendix of Theuns et al. (1998), except that here we integrate over each pixel rather than evaluating the kernel at the centre of the pixel. Kernel integration is much simplified by using a Gaussian kernel rather than the M4-spline used in GADGET, and we do so as described by Altay & Theuns (2013).

Each pixel generates a Gaussian absorption profile of the form

$$\tau = \tau_0 \exp(-v^2/b_{\rm T}^2) \quad (1)$$

$$b_{\rm T}^2 = \left(\frac{2k_{\rm B}\,T}{m_{\rm H}}\right) \quad (2)$$

$$\tau_0 = \sigma_0 \frac{c}{\pi^{1/2}\,b_{\rm T}}\,N_{\rm HI} \quad (3)$$

$$\sigma_0 = \left(\frac{3\pi\,\sigma_T}{8}\right)^{1/2} \lambda_0\,f\,, \quad (4)$$

where $v = v_{\rm z,pix} - v_{\rm z,part}$ is the velocity difference between the pixel and the particle in the z-direction, and $N_{\rm HI}$ is the neutral hy-

[1] There is an additional contribution from the finite resolution of the spectrograph.

drogen column density of the pixel[2]. The physical constant appearing in these equations are the speed of light, c, Boltzmann's constant, $k_{\rm B}$, the hydrogen mass, $m_{\rm H}$, and the Thompson cross section, σ_T. For the Lyman α transition, the wavelength and f-values are taken to be $\lambda_0 = 1215.6701$ Åand $f = 0.416$, see Menzel & Pekeris (1935). Since we are analysing cosmic gas at densities around the mean density, we do not need to use the more accurate Voigt profile.

While the simulation is running, we output those particles that contribute to one hundred randomly chosen sightlines, for every 10 per cent increase in the cosmic expansion factor. This allows us to account accurately for any redshift evolution in the generated mock sightlines. The computation of the mock sightlines only takes into account the Lyα transition. We leave the consideration of other transitions of the Lyman series for future work. In addition to computing τ, we record the optical-depth weighted temperature, peculiar velocity, and overdensity as a function of wavelength. Garzilli et al. (2015a) demonstrate (their figure 1) that the relation between optical depth weighted temperature and density follows that of the actual TDR.

In the next section, we analyse mock sightlines generated with and without noise. We intend to mimic the properties of some observed spectra, and for example we consider the properties of spectra measured with HIRES. Hence, mock sightlines with noise are obtained by convolving the transmission $\exp(-\tau)$ with a Gaussian profile with full width at half maximum, rebinning the sightlines into pixels of $W_v = 4\,{\rm km\,s^{-1}}$, $f_{\rm FWHM}$, equal to 6.6 km s^{-1} and adding random Gaussian noise corresponding to a chosen signal-to-noise per pixel at the continuum, S/N=100 or 30.

3 ANALYTICAL EXPRESSION FOR THE MINIMUM ABSORPTION LINE BROADENING

In Garzilli et al. (2015b) we provided an analytical expression for the minimum absorption line broadening, b, as a function of the over-density, Δ, associated to the line. Unfortunately Δ cannot be measured directly from the observed spectra. Hence, here we derived a relation between b and the central neutral hydrogen optical depth in an absorption line, τ_0.

We start from the expression of the optical depth as in Miralda-Escude & Rees (1993)

$$\begin{aligned}
\tau(u_0) &= \Sigma \int_{u_{\rm A}}^{u_{\rm B}} \frac{n_{\rm HI}}{1+z} \left|\frac{du}{dx}\right|^{-1} \sigma_\alpha du \\
\sigma_\alpha &= \sigma_0 \frac{c}{b_{\rm T}\sqrt{\pi}} e^{-\frac{(u-u_0)^2}{b_{\rm T}^2}} \\
\frac{du}{dx} &= \frac{H(z)}{1+z} + \frac{\partial v_{\rm pec}}{\partial x}\,,
\end{aligned} \tag{5}$$

where $n_{\rm HI}$ is the neutral hydrogen number density, x is the comoving spatial coordinate, u is the velocity along the line of sight, $u_{\rm A}$ and $u_{\rm B}$ are the extremes of the absorber expressed in velocity along the line of sight, σ_α is the Lyα cross-section profile, $b_{\rm T} = (2k_{\rm B}T/m_{\rm H})^{1/2}$ is the thermal Doppler broadening, T is the temperature of the gas, $v_{\rm pec}$ is peculiar velocity, z is the mean redshift associated to the absorber and $H(z)$ is the Hubble parameter at redshift z, the summation is made over multiple streams of x with the same u.

[2] In practice we integrate the Gaussian in Eq. 1 over a pixel, rather than evaluating it at the pixel centre.

We neglect peculiar velocities and we assume a Gaussian profile for the neutral hydrogen number density, $n^0_{\rm HI}\exp\left\{-(u-u_0)^2/b_\lambda^2\right\}$, where $n^0_{\rm HI}$ is the neutral hydrogen number density at the center of the line and b_λ is the width of Gaussian profile of $n_{\rm HI}$. Hence, the neutral hydrogen optical depth becomes

$$\tau(u) = \frac{\sigma_0 c n^0_{\rm HI}}{H(z)} \frac{b_\lambda}{b} e^{-\frac{(u-u_0)^2}{b^2}}\,, \tag{6}$$

where we will assume the line broadening to be equal to the 'minimal' line broadening

$$b \equiv b_{\rm min} = \left(b_{\rm T}^2 + b_\lambda^2\right)^{1/2}\,. \tag{7}$$

The width of the Gaussian profile for $n_{\rm HI}$ can be expressed as

$$b_\lambda = \lambda_{\rm F} \frac{H(z)}{2\pi}\,, \tag{8}$$

as in Garzilli et al. (2015b), where $\lambda_{\rm F}$ is the proper extent of the absorbing structure. Again as in Garzilli et al. (2015b), we make the ansatz that

$$\lambda_{\rm F} = f_{\rm J}\lambda_{\rm J}(\Delta)\,, \tag{9}$$

where $f_{\rm J}$ is a constant that parametrizes the time-dependent Jeans-smoothing of the gas density profiles (Gnedin & Hui 1998), and $\lambda_{\rm J}$ is the local Jeans length of an absorber (Schaye 2001). Here we use

$$\begin{aligned}
\lambda_{\rm J}(\Delta) &= \pi\left(\frac{40}{9}\right)^{1/2}\left(\frac{k_{\rm B}}{m_{\rm H}}\right)^{1/2}(1+z)^{-3/2} {H_0}^{-1}\mu^{-1/2}{\Omega_m}^{-1/2} \\
&\times\ T^{1/2}\Delta^{-1/2}\,,
\end{aligned} \tag{10}$$

where μ is the mean molecular mass, Ω_m is the matter density parameter and H_0 is the Hubble constant. In the following we will indicate with $\lambda^0_{\rm F}$ the proper extent of absorbing structure at the cosmic mean density.

We consider the TDR we have described in section 2.1. We make explicit how b and τ_0 depend on Δ, the temperature at cosmic mean density, T_0, the slope of the TDR, γ, the proper length of the absorbers of the Lyα forest, $\lambda_{\rm F}$, and the intensity of the hydrogen ionizing background, $\Gamma_{\rm HI}$

$$\begin{aligned}
\tau_0 &= \frac{\sigma_0 c n^0_{\rm HI}}{H(z)} \frac{b_\lambda}{\sqrt{b_{\rm T}^2 + b_\lambda^2}} \\
n^0_{\rm HI} &= \alpha_0 \frac{9}{128\pi^2}(m_{\rm H}G)^{-2}(2-Y)(1-Y)(1+z)^6 {H_0}^4 {\Omega_b}^2 \\
&\times\ {\Gamma_{\rm HI}}^{-1}\left(\frac{T_0}{10^4\,{\rm K}}\right)^{-0.76}\Delta^{2.76-0.76\gamma} \\
\alpha_0 &= 4\times 10^{-13}{\rm cm^3 s^{-1}}\,,
\end{aligned} \tag{11}$$

where Ω_b is the baryon density parameter, Y is the helium fraction by mass, G is the gravitational constant, α_0 is the recombination constant at $T = 10^4$ K. We do not provide an explicit the relation between τ_0 and b, but it can be computed by inverting numerically Eq. 11 with respect to Δ.

In Figure 1, we compare the distribution of the line broadening in the plane b-Δ and in the plane b-τ_0, to highlight their similarity. The error bars on the 10th and 50th percentiles of the b-distribution are computed by bootstrapping the mock spectra. The minimum line broadening is a difficult quantity to measure. It is possible in noiseless spectra to measure an arbitrary percentile of the distribution of the line broadening, but that can only approximate the minimum line broadening. For this reason, we adapt Eq. 7, which we have written for the minimum line broadening, to the case of a generic percentile of the line broadening distribution, $b_{\rm perc}$

$$b^2_{\rm perc} = \eta^2_{\rm perc}(b_T^2 + b_\lambda^2)\,, \tag{12}$$

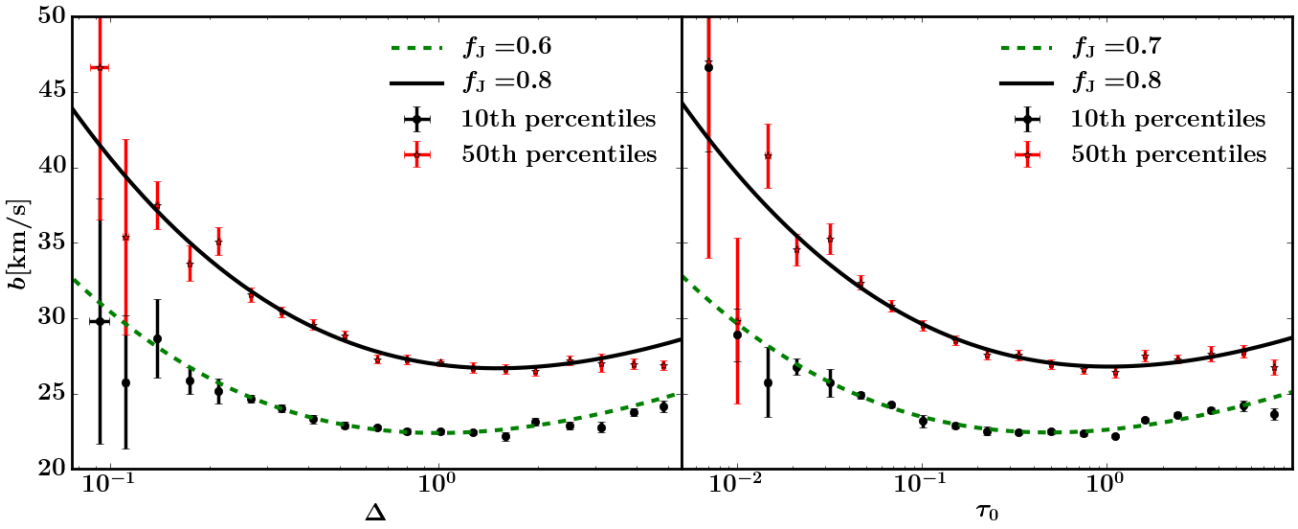

Figure 1. The line broadening, b, from 100 noiseless mock spectra versus the central density contrast, Δ (left panel), and the central neutral hydrogen optical depth, τ_0 (right panel), in the redshift interval $2.9 \leqslant z \leqslant 3.0$. The black dots (red stars) are the 10th (50th) percentiles of the b-distribution in the mock spectra. The error bars represent the 1-σ uncertainty on the percentiles. In the left panel, the green dashed (solid black) line is a fit of our expression for the line broadening, Eq. 12, to the 10th (50th) percentiles of the b-distribution divided in logarithmically and equally spaced intervals of Δ. The values of T_0 and γ are the result of the fit to the temperature-density relation, the values of f_J and η are the result of the fit of the b-Δ relation. In the right panel, we have presented the analogous fit to the percentiles of the b-distribution divided in intervals of τ_0. In the transition from b-Δ space to b-τ_0, the fitted values of f_J agree to 15%. Our analytical expression for the line broadening correctly describes both the lower bound and the median of line width distribution in our reference simulation, except for high values of τ_0, where the downturn in b is due to the onset of radiative cooling.

where $\eta_{\rm perc}$ is a constant that will depend on the chosen percentile of the b-distribution. This constant must be determined from simulations. Eq. 12 describes well both the 10th and the 50th percentiles of the absorption line broadening distribution up to $\tau_0 \sim 10$. Nevertheless, the values of f_J can differ in the fits to the b-Δ distribution or to b-τ_0 distribution. The discrepancy in f_J between these two distribution can be up to $\sim 15\%$. For $\tau_0 \gtrapprox 10$ radiative cooling becomes relevant, although the precise value of τ_0 for which this occurs depends on the specific values of T_0, γ, λ_F and $\Gamma_{\rm HI}$. In this work we only consider the case of power-law TDR, but we intend to address the problem of a general TDR in a future publication.

4 METHOD FOR RECONSTRUCTING THE ABSORPTION LINE BROADENING

In this section we will discuss how to reconstruct the minimum line broadening from spectra with noise, and then how to estimate the IGM temperature and width of the filaments in the IGM. In the presence of noise and instrumental broadening, we cannot apply directly the formalism that we have developed in Garzilli et al. (2015b) for measuring the line broadening occurring in the Ly α forest to observed quasar spectra. In fact, the computation of the second derivative in the measurement of b is not stable under noise. In order to smooth out the noise, we first fit the sightlines with a superposition of Voigt profiles, and then apply the procedure we have already developed for noiseless sightlines on the spectra reconstructed from their Voigt profile decompositions, and determine b and τ_0 for each absorber. We then apply Eq. (12). In this section, we consider the case of mock lines to which we added noise with S/N=100. We use a sample size of a total 500 sightlines for each considered redshift interval, each spectrum has a length of $25\,c$Mpc. If we analyze together all the signal coming from bins in redshift of $\Delta z = 0.1$, then for redshifts ranging from $z = 4$ to 2, 500 sightlines correspond to a number of Lyman α quasar spectra varying from 180 to 85.

4.1 Reconstructing the line broadening in the Lyα forest

We attempt to remove the noise in the mock sightlines, by fitting the Lyα stretch in the mock sightlines with noise with VPFIT (Carswell et al. 1987; Webb 1987). The full spectrum flux is divided into intervals of variable length, between 10 and 15 Å. We start from the minimum wavelength in the Lyα stretch, λ_1, then we search for the maximum of the flux in the interval $[\lambda_1 + 10\,\text{Å}, \lambda_1 + 15\,\text{Å}]$, the wavelength corresponding to the maximum flux will be λ_2. Then, the maximum of the flux in the interval $[\lambda_2 + 10\,\text{Å}, \lambda_2 + 15\,\text{Å}]$ is identified and the corresponding wavelength will be λ_3. This process is repeated until the end of the spectrum, has been reached. In this way the spectrum is subdivided into intervals of variable length. Each interval of transmitted flux is fit independently with VPFIT. The stopping criteria that we have considered is given by the change of the chi-square, $\Delta\chi^2$, between iteration steps. If $\chi^2 < 15$ then the iterations terminates if $\Delta\chi^2/\chi^2 < 5 \times 10^{-4}$, otherwise if $\Delta\chi^2/\chi^2 < 5 \times 10^{-3}$. The flux is also reconstructed separately for each independent stretch. We do not attempt to perform a full Voigt-profile fitting of the entire Lyα forest, because of the long computing time required for fitting automatically the entire Lyα forest in one batch. We are only interested in a noiseless reconstruction of the flux in the minimum χ^2 sense. On the reconstructed optical depth we apply the 'peak identification' method and estimate the line broadening as described in Garzilli et al. (2015b) for the case of noiseless sightlines.

In Figure 2 we show a comparison between the 10th and 50th percentiles of the b-distribution for noiseless sightlines and for the reconstructed flux for the case of high and low S/N. We have considered 500 sightlines in the redshift interval $2.9 \leqslant z \leqslant 3.0$. We would like to measure the minimum line broadening in the sightlines, hence ideally we would like to consider the 10th-percentiles of the line broadening. Nevertheless, we can see that qualitatively the 10th percentiles are not reconstructed very well in the sightlines with noise. Instead, the 50th percentiles (or medians) of the line broadening are reconstructed over a larger τ_0 range. For this reason, in the following we will characterize the line broadening by considering the 50th percentiles of the b-distribution, rather than the 10th.

In Figures 3 we compare the PDF of the b-distribution as found in the noiseless sightlines and in the sightlines with noise, for two distinct intervals in τ_0. For $0.08 \leqslant \tau_0 \leqslant 0.12$, the PDF of the reconstructed b is much flatter then the PDF of the noiseless b, and the two PDFs do not match each other overall. The number density of lines in the noiseless sightlines is $n_{\rm noiseless} = 9.4 \times 10^{-4}\,{\rm s\,km^{-1}}$, whereas the number of lines per length in the sightlines with noise is $n_{\rm noise} = 8 \times 10^{-4}\,{\rm s\,km^{-1}}$. For $0.8 \leqslant \tau_0 \leqslant 1.2$ the PDFs of the reconstructed and noiseless b are quite similar, they both exhibit a sharp cut-off for low values of b and a declining tail for large values of b. We conclude that the line broadening is reconstructed less accurately in correspondence of the smallest values of τ_0. The number of lines per length is $n_{\rm noiseless} = 7 \times 10^{-4}\,{\rm s\,km^{-1}}$ and $n_{\rm noise} = 1 \times 10^{-4}\,{\rm s\,km^{-1}}$. We can determine the 50th percentiles of b well for $\tau_0 \sim 1$.

4.2 Estimation of the IGM parameters

We have considered the estimation of the IGM parameters over a redshift interval $z \in [2.9, 3.6]$, with a redshift step $\Delta z = 0.1$.

We intend to estimate T_0, γ, $\lambda_{\rm F}^0$ and $\Gamma_{\rm HI}$. T_0 and γ are the parameters of the TDR, and they have been the object of many studies in the past, whereas the role of $\lambda_{\rm F}$ in setting the line broadening has been recognized only relatively recently, $\Gamma_{\rm HI}$ is a parameter that is usually kept fixed to a value. We have decided to vary $\Gamma_{\rm HI}$ because it affects the optical depth. In fact, when $\Gamma_{\rm HI}$ is inferred from observations, T_0 is assumed. In order to get an estimate of all the parameters, we fit the measured 50th percentile of the b-distribution from the sightlines with noise with the model $b(\tau, T_0, \gamma, \lambda_{\rm F}^0, \Gamma_{\rm HI})$, our analytical formula for line broadening, Eq. (12). We have chosen the interval for the reconstructed central optical depth $\tau_0 = [0.1, 4]$, as to exclude the region affected by cooling and by noise. We divide the central optical depth into equispaced logarithmic intervals, and we compute the median of the line broadening for each central optical depth bin. We indicate the resulting collection of central optical depth and median line broadening values with $\hat{\tau}_i, \hat{b}_i$, where i is index that varies on the bins of the central optical depth. We also estimate the 1-σ error on $\hat{b}_i$, $\sigma(\hat{b}_i)$. The errors are estimated by bootstrapping the line of sights, rather than the absorption lines. The theoretical model is indicated with the notation $b_i(T_0, \gamma, \lambda_{\rm F}^0, \Gamma_{\rm HI}) = b(\tau_i, T_0, \gamma, \lambda_{\rm F}^0, \Gamma_{\rm HI})$. The constant η_{50th}, appearing in Eq. (12), has been calibrated using our reference simulation, separately for each redshift interval, as in Table 1.

In order to perform the fit, we compute the chi-squared function, χ^2, defined as $\chi^2 = \sum_i \left(b_i(T_0, \gamma, \lambda_{\rm F}^0, \Gamma_{\rm HI}) - \hat{b_i}\right)^2 / \sigma(\hat{b_i})^2$, where $b(T_0, \gamma, \lambda_{\rm J}^0, \Gamma_{\rm HI})$ is the line broadening as computed from Eq. (12), $\hat{b}$ is the 50th percentile of b-distribution. We compute the corresponding likelihood function by $\mathcal{L} = \exp(-\chi^2/2)$ and maximize the likelihood by using Montepython (Audren et al. 2013) and CosmoMC (Lewis & Bridle 2002). We have chosen logarithmic priors on T_0, $\Gamma_{\rm HI}$ and $\lambda_{\rm F}^0$ and a flat prior on γ, which are summarized in Table 2.

Table 1. Values of η_{50th}, appearing in Eq. (12), calibrated from our reference simulation as a function of redshift, z.

z	η_{50th}
2.95	1.32
3.05	1.27
3.15	1.25
3.25	1.28
3.34	1.26
3.45	1.26
3.56	1.25

Table 2. Prior ranges considered for the parameter of the maximum likelihood analysis, used for fitting the mock median line broadening data to the model given by Eq. (12). We have chosen logarithmic priors on T_0, $\Gamma_{\rm HI}$ and $\lambda_{\rm F}^0$ and a linear prior on γ. Here and in the rest of the paper, log indicates the logarithm in base 10.

	min	max
$\log(T_0[{\rm K}])$	0	5
γ	1	2
$\log(\lambda_{\rm F}^0[{\rm cMpc}])$	-3	3
$\log(\Gamma_{\rm HI}[{\rm s^{-1}}])$	-13	-11

Before presenting the joint fit of all parameters, we show in Figure 4 how the minimal line broadening is affected by each parameter independently, using our analytical model of the line broadening in Eq. (12). Changing T_0 is almost equivalent to changing the line broadening by a multiplicative factor. Changing $\lambda_{\rm F}^0$ mostly affects the line broadening at small τ_0. Changing γ affects the slope of the line broadening at all τ_0. Changing $\Gamma_{\rm HI}$ has the effect of changing the neutral fraction of hydrogen, hence it affects the Δ-τ_0 relation, and it shifts the position in the minimum of the b-τ_0 relation. The effect of $\Gamma_{\rm HI}$ is only to shift the curves of line broadening left to right, but not up and down. We can expect some degeneracies between the estimated parameters in the final analysis: γ and $\Gamma_{\rm HI}$ appear to be correlated, T_0 and γ appear to be anti-correlated, T_0 and $\lambda_{\rm F}^0$ anti-correlated, $\lambda_{\rm F}^0$ and $\Gamma_{\rm HI}$ correlated.

The results of the parameters estimation are shown in Figure 5, where the IGM parameters are estimated independently for each redshift bin. The number of data points is 14 for each redshift interval and the number of free parameters is 4 for each redshift bin. The estimates of T_0 and $\lambda_{\rm F}^0$ agree with the known values from the simulation at the 1-σ level, whereas γ agrees with the simulation at the 1-σ level for all the redshift bins except one, where it agrees at the 2-σ level. For $\Gamma_{\rm HI}$ there are no constraints. In Figure 6, we show the likelihood contours for the parameters estimated for the redshift interval $2.9 \leqslant z \leqslant 3.0$, here the correlation between the measured values of $\Gamma_{\rm HI}$ and $\lambda_{\rm F}^0$, and the anti-correlations between T_0 and γ, $\lambda_{\rm F}^0$ and T_0, and γ and $\Gamma_{\rm HI}$ are apparent. Those degeneracies are in agreement with the behavior of the minimum line broadening with the IGM parameters shown in Figure 4. Especially, the expected anti-correlations in $\lambda_{\rm F}^0$-T_0 and γ-T_0 are visible and also the correlation between $\Gamma_{\rm HI}$ and $\lambda_{\rm F}^0$.

In order to improve the constraining power of our method, we also consider the case that $\lambda_{\rm F}^0$ is kept fixed across distinct redshift bins. This reflect the physical observation that while the IGM tem-

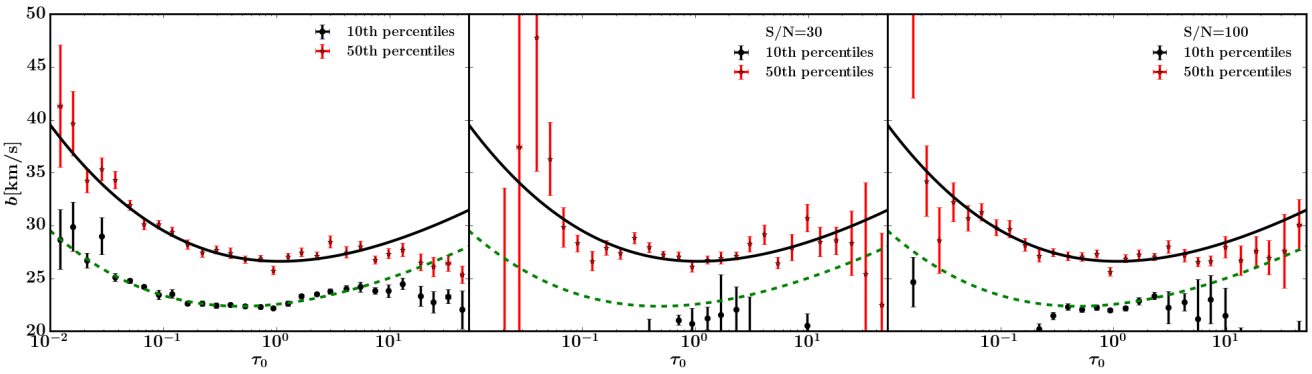

Figure 2. Comparison between the percentiles of the distribution of line broadening in the noiseless sightlines, and in the sightlines reconstructed with VPFIT, in the case of high and low signal-to-noise, for the redshift range $2.9 \leqslant z \leqslant 3.0$. We have considered 500 lines of sight, each of length 25 cMpc . The left panels correspond to the noiseless case, the middle panel corresponds to the sightlines with noise with S/N=30, and the right panel to S/N=100. The black dots (red stars) are the 10th (50th) percentiles of the line broadening as a function of the central optical depth, τ_0. The green dashed (black solid) line is the result of the fit of Eq.(12) to the 10th (50th) percentiles of the b-distribution, where T_0 and γ are inferred from the temperature-density relation, and f_J and η are free parameters in the fit. In the case of reconstructed sightlines with VPFIT, the 10th percentiles of the b-distribution are very poorly reconstructed. In contrast, the 50th percentiles of the b-distribution are reconstructed well over a larger range of τ_0. The robustness under reconstruction with VPFIT makes the 50th percentiles more suitable for the study of the properties of the IGM.

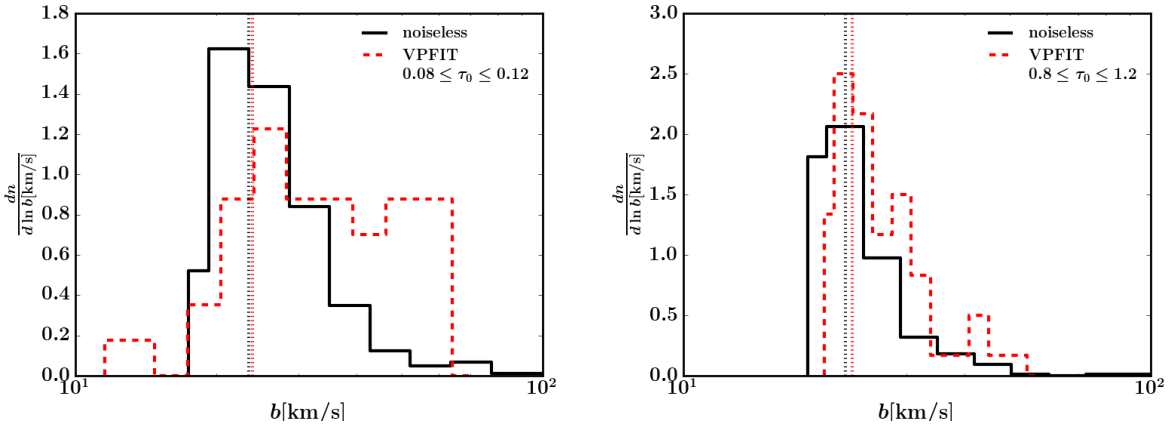

Figure 3. The probability density distribution of the line broadening, b, for two values of the central optical depth, τ_0, for 100 mock sightlines without noise and with noise (S/N=100). The left panel refers to the line broadening corresponding to $0.08 \leqslant \tau_0 \leqslant 0.12$, the right panel to $0.8 \leqslant \tau_0 \leqslant 1.2$. The black solid line is the PDF in the noiseless sightlines, the red dashed line is the one from the sightlines with noise. The black vertical line corresponds to the 10th percentile of the b-distribution in the noiseless sightlines, the red dashed vertical line corresponds to the 10th percentile of the b-distribution in the sightlines with noise.

perature could in principle vary abruptly due to the appearance of new ionizing sources, the size of the filaments is set by the dynamical effect of pressure smoothing, and will vary more smoothly than the temperature. We choose to keep the comoving λ_F^0 fixed over $2.9 \leqslant z \leqslant 3.3$ and $3.3 \leqslant z \leqslant 3.6$ in the parameters estimation. This means that, in the minimization of the χ^2, the thermal state parameter were free to vary for each redshift bin, whereas the comoving length was kept the same in all redshift bins. We show the results of this analysis in Figure 7. The resulting error bars on all the parameters are significantly smaller than in the previous analysis. Nonetheless, there is some tension between the measurements and the true values of the parameters known from the reference simulation, for T_0, $\Gamma_{\rm HI}$, and λ_F^0.

We also can measure the mean flux independently from the line broadening. We show the case of the analysis keeping $\Gamma_{\rm HI}$ fixed in Figure 8. Doing so decreases the uncertainty on all the estimated parameters. In the case of real data, we would first fix T_0 and γ and then measure $\Gamma_{\rm HI}$ by rescaling the predicted $\tau_{\rm eff}$ to match the observed mean flux decrement. Then, we would fix $\Gamma_{\rm HI}$ and measure T_0 and γ. We would use these resulting measurements as input for a new measurements of $\Gamma_{\rm HI}$. We would iterate this process until convergence.

5 CONCLUSIONS

We have described a new method to measure the IGM temperature and the widths of the filaments that are responsible for the absorption in the Lyα forest, based on the description of the minimum line broadening that we have developed in Garzilli et al. (2015b). In the

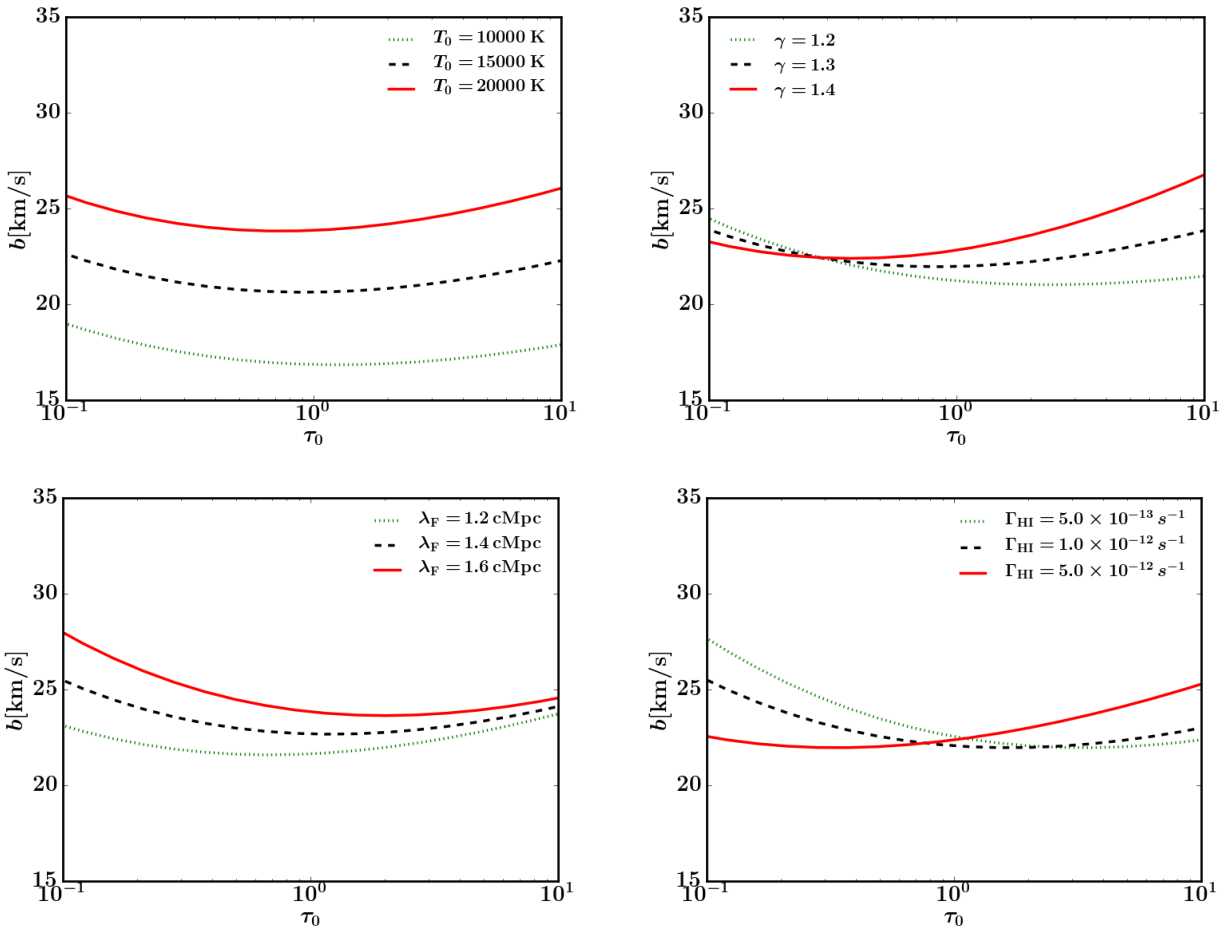

Figure 4. The effect on the line broadening of varying T_0, γ, λ_F^0 and Γ_{HI} independently. The line broadening is computed from Eq. (11) for $z = 3.0$ (with $\eta = 1$).

original formulation, we derived a relation between the minimum line broadening of the Lyα forest and the over-density, Δ. Because Δ is a quantity that cannot be measured directly in observed quasar spectra, we reformulated the minimum line broadening description in terms of the central line optical depth, τ_0, that can be measured directly.

In this work we considered the problem of reconstructing the line broadening in spectra with noise and finite instrumental resolution. We used automatic Voigt profile decompositions by VPFIT to reconstruct noiseless spectra from noisy data, and to this reconstructed spectra we applied the method for finding the lines and computing the line broadening for noiseless sightlines that we described in Garzilli et al. (2015b). We have found that the 10th percentiles of the line broadening are not very well reconstructed for the smallest values of τ_0, whereas the median line broadening is more robust.

We applied our method to a sample of mock sightlines extracted from our reference simulation with low and high signal to noise. We calibrated our method to our reference numerical simulation, by determining the multiplying factor needed to match the median line broadening to the minimal line broadening. It is difficult to draw a comparison of our method with the methods that have been applied in the past, due to the conservative approach we have employed. We used very conservative priors on the parameters in our analysis, and we varied parameters that are held fixed. We conclude that our method allows us to reconstruct the properties of the IGM, such as the temperature and size of the expanding filaments at the cosmic mean density, and marginally the photo-ionisation rate of neutral hydrogen. We have also shown that keeping the comoving size of the filaments constant over large redshift interval improves the constraining power of our method.

We aim to apply this method to observed quasar spectra, in order to obtain new measurements of the IGM temperature and of the sizes of the absorbing structures, combining our method on line broadening that we have described here with the constraints from the measurement of the mean optical depth. These measurements will be presented in a forthcoming paper.

ACKNOWLEDGEMENT

The authors thanks Michele Fumagalli for reading and commenting an earlier version of the draft. AG thanks D-ITP for supporting this research. This work used the DiRAC Data Centric system at Durham University, operated by the Institute for Computational Cosmology on behalf of the STFC DiRAC HPC Facility (www.dirac.ac.uk). This equipment was funded by BIS National E-infrastructure capital grant ST/K00042X/1, STFC capital grants ST/H008519/1 and ST/K00087X/1, STFC DiRAC Opera-

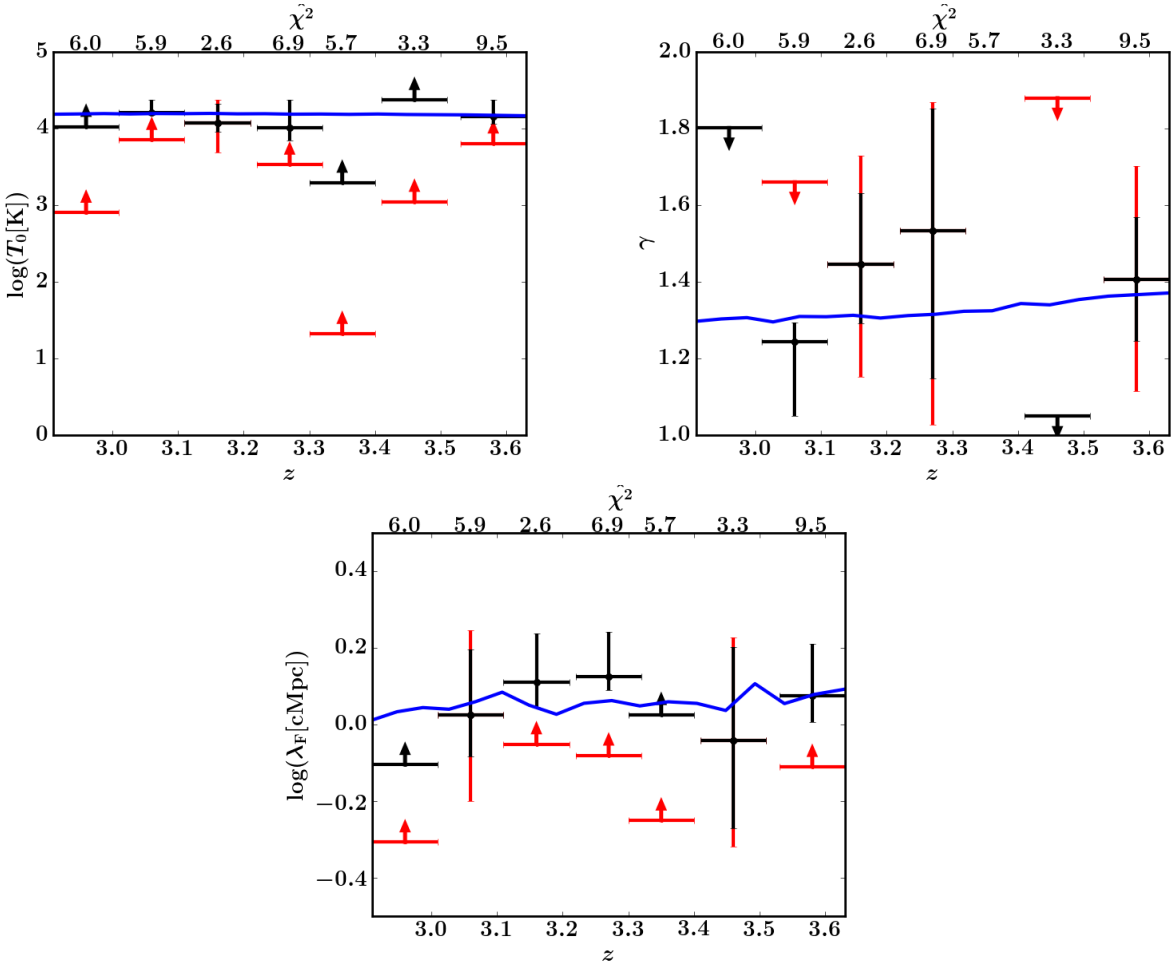

Figure 5. The result of estimation of T_0, γ and λ_F^0 for the case the IGM parameters are estimated independently for each redshift bin. There are no constraints on Γ_HI. The black error bars indicate the 1-σ errors, and the red error bars are the 2-σ contours. The black (red) bars with arrows are 1-σ (2-σ) lower or upper limit. The number on the top of each panel show the resulting best-fitting χ^2 for each redshift bin. The solid blue line are the values of the parameters measured from the simulations.

tions grant ST/K003267/1 and Durham University. DiRAC is part of the National E-Infrastructure.

APPENDIX A: A COMPARISON WITH TRADITIONAL VOIGT PROFILE FITTING

We consider the reconstruction of percentiles of line broadening obtained from Voigt profile fitting, which has been widely used in the literature. Voigt profile fitting has been considered in Schaye et al. (1999); Schaye et al. (2000); Ricotti et al. (2000); McDonald et al. (2001); Bolton et al. (2012); Rudie et al. (2012) for measuring the IGM temperature, and it is the only line decomposition technique applied so far to the Lyα forest, using a variety of codes like VPFIT, FITLYMAN (Fontana & Ballester 1995) or AUTOVP (Dave et al. 1997). Voigt profile fitting is a global fitting method that implies fitting the entire shape of the transmitted flux. Hence, it is sensitive to the clustering of the absorbers in the Lyα forest, in other words, it is sensitive to the underlying density distribution of the gas. In fact, some Voigt profiles with very small b_VPFIT are present, because they improve the overall convergence of the fit. Instead, our 'peak decomposition' only measures the line broadening at "local maxima" in the optical depth. We have applied Voigt profile fitting to our mock sightlines with noise using VPFIT (Carswell et al. 1987; Webb 1987). In Figure A1 we show the resulting b_VPFIT-N_HI distribution, and compare it with the amount of line broadening described by Eq. 12. The upturn of the b-N_HI distribu-

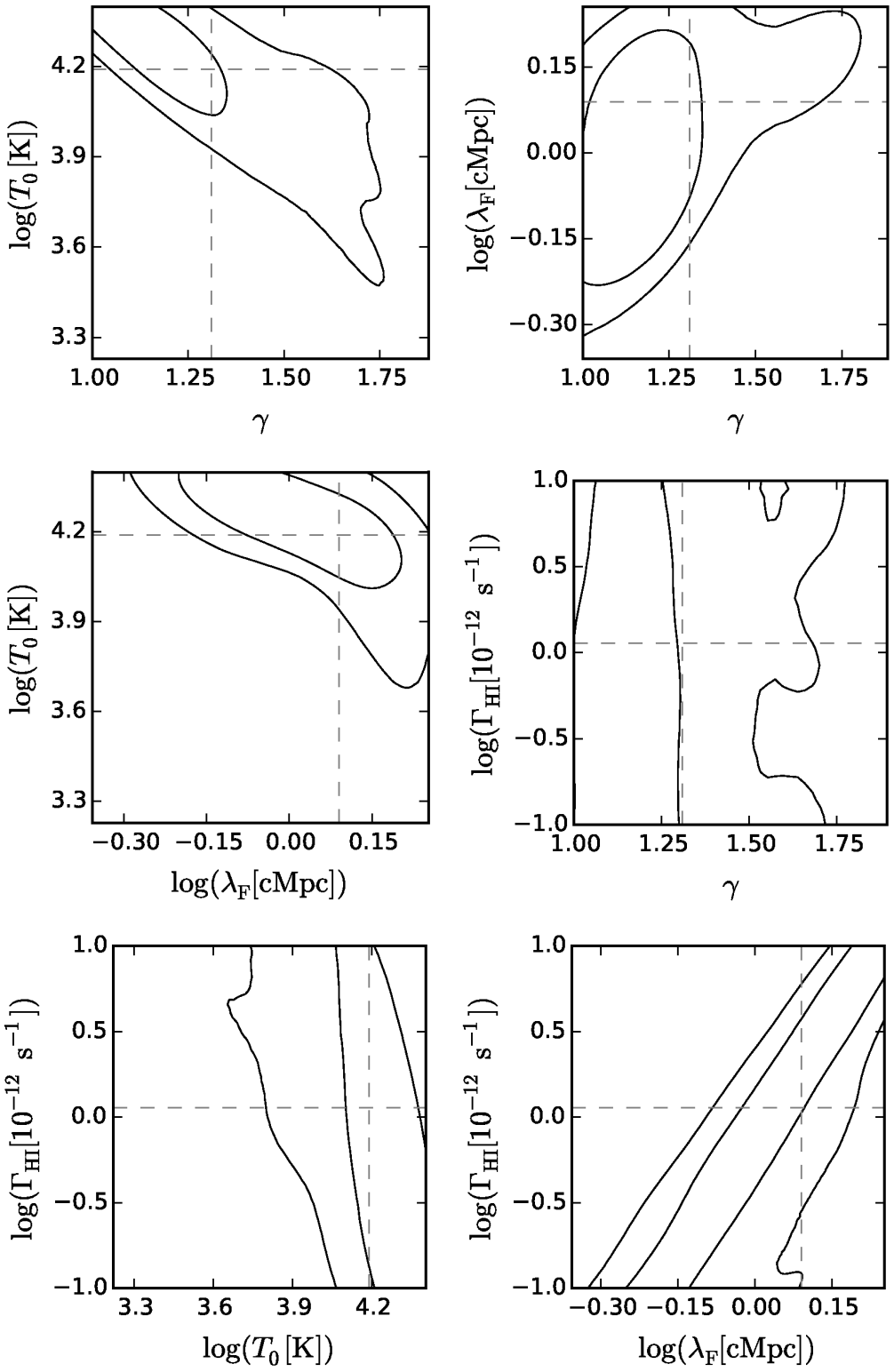

Figure 6. The likelihood contours for the analysis in Figure 5 at $z = 3.06$. The measured value of T_0 is anti-correlated with both γ and λ_F^0. The value of Γ_{HI} is correlated with λ_F^0. The origin of these degeneracies can be understood by comparing to Figure 4. The true values in the simulations are represented by the horizontal and vertical dashed lines.

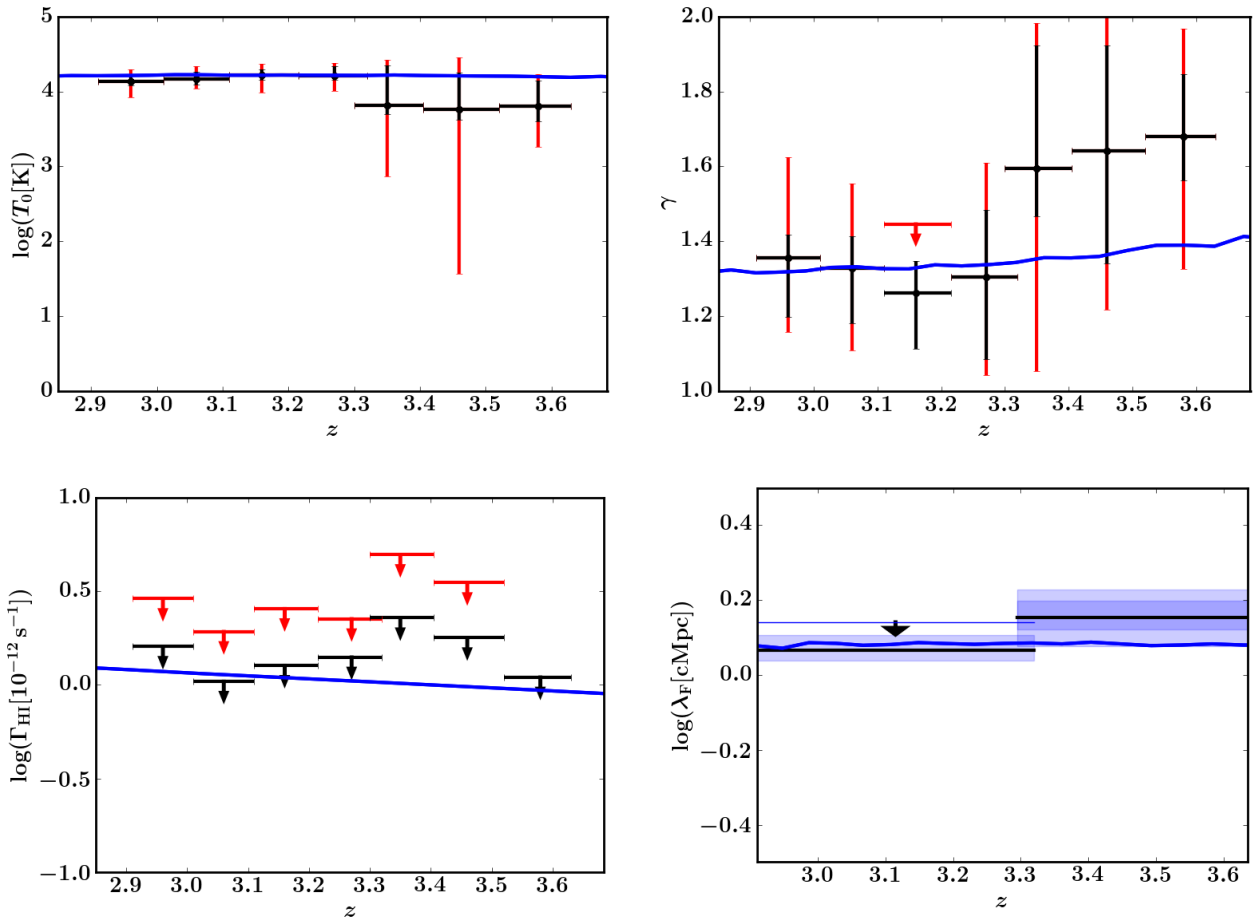

Figure 7. The result of estimation of T_0, γ, $\Gamma_{\rm HI}$ and $\lambda_{\rm F}^0$, where $\lambda_{\rm F}^0$ is kept constant across the redshift interval $2.8 \leqslant z \leqslant 3.3$ and $3.3 \leqslant z \leqslant 3.6$. Same conventions as in Figure 5. The light and dark bands in the bottom right panel are the 1-σ and 2-σ contours for $\lambda_{\rm F}^0$.

tion that is expected for small $N_{\rm HI}$ is visible neither in the 10th nor 50th percentiles of the $b_{\rm VPFIT}$ distribution.

APPENDIX B: CONSIDERING LOWER S/N

In Figure B1 we show the results of the parameters estimation for the case of a low signal-to-noise sample of spectra (S/N=30) for the central optical depth interval $\tau_0 \in [0.3, 4]$ (that is different from the optical depth interval that we have chosen for the high signal-to-noise sample). The results are similar to the ones found in the high signal-to-noise case, but with larger error bars.

We conclude that our method also works with lower signal to noise spectra, and it is hence applicable to existing spectra.

REFERENCES

Altay G., Theuns T., 2013, MNRAS, 434, 748
Audren B., Lesgourgues J., Benabed K., Prunet S., 2013, JCAP, 1302, 001
Becker G. D., Bolton J. S., Haehnelt M. G., Sargent W. L. W., 2011, MNRAS, 410, 1096
Bolton J. S., Haehnelt M. G., Viel M., Springel V., 2005, MNRAS, 357, 1178
Bolton J. S., Viel M., Kim T.-S., Haehnelt M. G., Carswell R. F., 2008, MNRAS, 386, 1131
Bolton J. S., Becker G. D., Raskutti S., Wyithe J. S. B., Haehnelt M. G., Sargent W. L. W., 2012, MNRAS, 419, 2880
Calura F., Tescari E., D'Odorico V., Viel M., Cristiani S., Kim T.-S., Bolton J. S., 2012, MNRAS, 422, 3019
Cantalupo S., Arrigoni-Battaia F., Prochaska J. X., Hennawi J. F., Madau P., 2014, Nature, 506, 63
Carswell R. F., Webb J. K., Baldwin J. A., Atwood B., 1987, ApJ, 319, 709
Crain R. A., et al., 2015, MNRAS, 450, 1937
Dave R., Hernquist L., Weinberg D. H., Katz N., 1997, Astrophys. J., 477, 21
Desjacques V., Nusser A., 2005, Mon. Not. Roy. Astron. Soc., 361, 1257
Faucher-Giguère C.-A., Lidz A., Hernquist L., Zaldarriaga M., 2008, ApJ, 688, 85
Fontana A., Ballester P., 1995, The Messenger, 80, 37
Fumagalli M., Haardt F., Theuns T., Morris S. L., Cantalupo S., Madau P., Fossati M., 2017, MNRAS, 467, 4802
Garzilli A., Bolton J. S., Kim T.-S., Leach S., Viel M., 2012, MNRAS, 424, 1723
Garzilli A., Theuns T., Schaye J., 2015a, MNRAS, 450, 1465
Garzilli A., Theuns T., Schaye J., 2015b, Mon. Not. Roy. Astron. Soc., 450, 1465
Garzilli A., Boyarsky A., Ruchayskiy O., 2017, Phys. Lett., B773, 258
Gnedin N. Y., Hui L., 1998, MNRAS, 296, 44
Gunn J. E., Peterson B. A., 1965, ApJ, 142, 1633
Haardt F., Madau P., 1996, ApJ, 461, 20
Haardt F., Madau P., 2001, in Neumann D. M., Tran J. T. V., eds, Clusters of Galaxies and the High Redshift Universe Observed in X-rays.

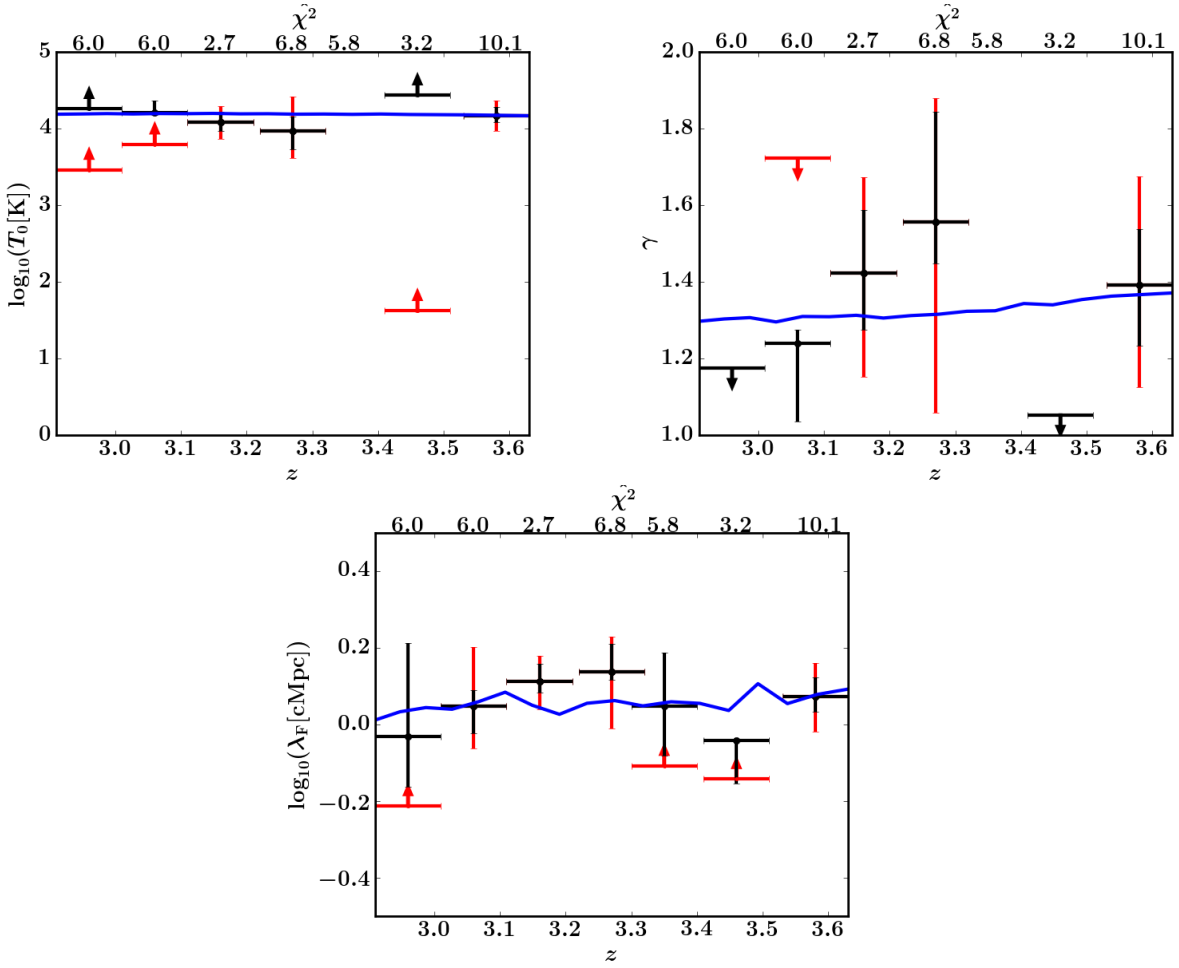

Figure 8. The result of estimation of T_0, γ and λ_F^0, when Γ_HI is kept fixed to the values of the Eagle simulation. Same conventions as in Figure 5. Keeping Γ_HI fixed reduces the error bars on the parameters.

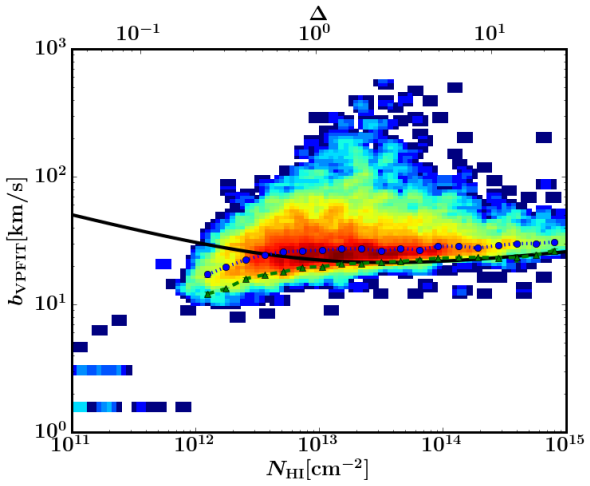

Figure A1. The distribution of line broadening as obtained from VPFIT, b_VPFIT, versus the neutral hydrogen column density, N_HI. The color scheme encodes the number density of the lines in the b_VPFIT-N_HI plane. The blue dots (green triangles) connected by a dotted (dashed) line are the 50th (10th) percentiles of the b_VPFIT-distribution in equally spaced logarithmic intervals of N_HI. The solid black line is the line of minimum line broadening, from Eq. 25 Garzilli et al. (2015b). Both the 10th and the 50th percentiles of the b_VPFIT-distribution turn towards low values of b_VPFIT for low values of N_HI, these percentiles look different from the case of b measured with our method, shown in Figure 2, where the percentiles of the b distribution turn towards high values of b for low values of τ_0, as expected theoretically.

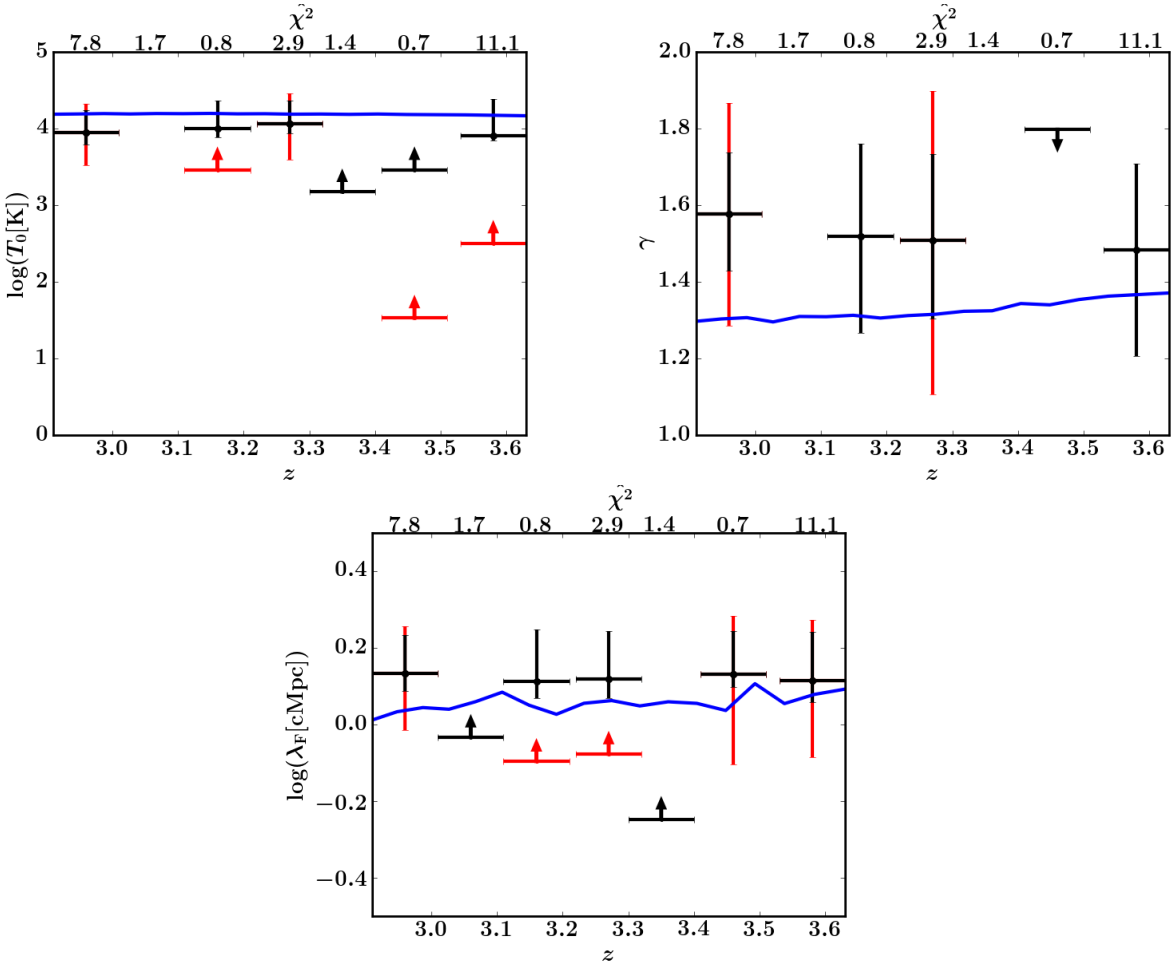

Figure B1. The results of T_0, γ and λ_F^0 estimation for the case of lower signal-to-noise spectra (S/N=30), each redshift bin is analyzed independently. The b-τ_0 relation is fitted in the interval $\tau_0 \in [0.3, 4]$. There are no constraints on Γ_HI. Same conventions as in Fig. 5.

(arXiv:astro-ph/0106018)
Hiss H., Walther M., Hennawi J. F., Oñorbe J., O'Meara J. M., Rorai A., 2017, preprint, (arXiv:1710.00700)
Hui L., Gnedin N. Y., 1997, MNRAS, 292, 27
Hui L., Gnedin N. Y., Zhang Y., 1997, ApJ, 486, 599
Kirkman D., et al., 2005, MNRAS, 360, 1373
Kulkarni G., Hennawi J. F., OÃśorbe J., Rorai A., Springel V., 2015, Astrophys. J., 812, 30
Lewis A., Bridle S., 2002, Phys. Rev., D66, 103511
Lidz A., Faucher-Giguère C.-A., Dall'Aglio A., McQuinn M., Fechner C., Zaldarriaga M., Hernquist L., Dutta S., 2010, ApJ, 718, 199
McAlpine S., et al., 2016, Astronomy and Computing, 15, 72
McDonald P., Miralda-Escudé J., 2001, ApJ, 549, L11
McDonald P., Miralda-Escudé J., Rauch M., Sargent W. L. W., Barlow T. A., Cen R., 2001, ApJ, 562, 52
Meiksin A. A., 2009, Reviews of Modern Physics, 81, 1405
Meiksin A., White M., 2004, MNRAS, 350, 1107
Menzel D. H., Pekeris C. L., 1935, MNRAS, 96, 77
Miralda-Escude J., Rees M. J., 1993, MNRAS, 260, 617
Peeples M. S., Weinberg D. H., Dave R., Fardal M. A., Katz N., 2010, Mon. Not. Roy. Astron. Soc., 404, 1281
Planck Collaboration et al., 2014, A&A, 571, A16
Rauch M., et al., 1997, ApJ, 489, 7
Ricotti M., Gnedin N. Y., Shull J. M., 2000, ApJ, 534, 41
Rorai A., Hennawi J. F., White M., 2013, ApJ, 775, 81
Rorai A., et al., 2017, preprint, (arXiv:1704.08366)
Rudie G. C., Steidel C. C., Pettini M., 2012, ApJ, 757, L30
Sanderbeck P. R. U., D'Aloisio A., McQuinn M. J., 2016, Mon. Not. Roy. Astron. Soc., 460, 1885
Schaller M., Dalla Vecchia C., Schaye J., Bower R. G., Theuns T., Crain R. A., Furlong M., McCarthy I. G., 2015, MNRAS, 454, 2277
Schaye J., 2001, ApJ, 559, 507
Schaye J., Theuns T., Leonard A., Efstathiou G., 1999, MNRAS, 310, 57
Schaye J., Theuns T., Rauch M., Efstathiou G., Sargent W. L. W., 2000, Mon. Not. Roy. Astron. Soc., 318, 817
Schaye J., Crain R. A., Bower R. G., etcetera 2015, MNRAS, 446, 521
Seljak U., Makarov A., McDonald P., Trac H., 2006, Phys. Rev. Lett., 97, 191303
Springel V., 2005, MNRAS, 364, 1105
Theuns T., Zaroubi S., 2000, MNRAS, 317, 989
Theuns T., Leonard A., Efstathiou G., Pearce F. R., Thomas P. A., 1998, MNRAS, 301, 478
Theuns T., Schaye J., Haehnelt M. G., 2000, MNRAS, 315, 600
Viel M., Haehnelt M. G., 2006, Mon. Not. Roy. Astron. Soc., 365, 231
Viel M., Bolton J. S., Haehnelt M. G., 2009, MNRAS, 399, L39
Webb J. K., 1987, PhD thesis, PhD thesis, Univ. Cambridge, 1987.
Wiersma R. P. C., Schaye J., Smith B. D., 2009a, MNRAS, 393, 99
Wiersma R. P. C., Schaye J., Theuns T., Dalla Vecchia C., Tornatore L., 2009b, MNRAS, 399, 574
Zaldarriaga M., Hui L., Tegmark M., 2001, ApJ, 557, 519